A Model for Concentric Tube Continuum Robots Under Applied Wrenches

D. Caleb Rucker, *Student Member, IEEE,* Bryan A. Jones, *Member, IEEE,*
and Robert J. Webster III, *Member, IEEE*

Abstract— **Continuum robots made from telescoping pre-curved elastic tubes enable base-mounted actuators to specify the curved shapes of robots as thin as standard surgical needles. While free space beam mechanics-based models of the shape of these 'active cannulas' exist, current models cannot account for external forces and torques applied to the cannula by the environment. In this paper we apply geometrically exact beam theory to solve the statics problem for concentric-tube continuum robots. This yields the equivalent of forward kinematics for an active cannula with general tube precurvature functions and arbitrarily many tubes, under loading from a general wrench distribution. The model achieves average experimental tip errors of less than 3 mm over the workspace of a prototype active cannula subject to various tip forces.**

I. INTRODUCTION

An active cannula is a robot made from concentric elastic tubes that are each precurved, as shown in Figure 1. As the tubes are axially rotated and translated at their bases, the active cannula changes shape via elastic tube interaction. Generating bending from tube interaction in this way enables a large variety of possible shapes in a continuum robot with a diameter comparable to a standard surgical needle. These characteristics have led to many proposed minimally invasive surgical applications for active cannulas, including use in fetal procedures, the lung, the heart, and in transnasal and transgastic surgeries, among others (see [1] for an overview). While some of these applications, such as manipulating a fiber optic laser in the lung [2], may be accomplished with existing free-space models, in many foreseeable applications it will be useful for the cannula to intentionally manipulate tissue by retracting it, cutting it, dissecting it, traveling through it like a needle, etc. In such cases the cannula will experience external loading which may significantly change its shape. To control the position and applied force of the cannula under these conditions, a model of cannula shape under load is needed, which is our objective in this paper.

Recently, models accounting for external loading have been developed for larger-scale continuum robots, such as the pneumatic robot modeled with Cosserat rod theory by Trivedi et al. [3]. Gravagne, et al. used beam theory to derive the large deflection dynamics of a tendon driven continuum robot [4]. While our work draws upon similar geometrically exact beam theory as [3] and [4], an active cannula presents a fundamentally different problem because there are many elastica to consider rather than only one. While the concentric tubes are constrained to a common backbone curve, individual tubes can undergo torsion independent of each other. This precludes use of the above models, which cannot account for multiple tubes interacting in the backbone.

Substantial prior work has been done in active cannula modeling, but all models to date apply only in free space, and cannot account for external loads. Free space cannula models have been developed in parallel by several groups over the past few years. Terayama et al. [5] modeled the kinematics of curved tubes, but not the mechanics. Webster et al. [6] and Sears and Dupont [7], [8] included beam bending using Bernoulli-Euler beam mechanics. Torsional effects were added to the modeling framework in straight transmissions [6], [9], and then in curved sections of a two-tube cannula with circular precurvature [10], [11]. The latest model advancements generalize to arbitrarily many tubes and variable precurvature using energy minimization [12], [13] and other methods of classical rod theory [11]. While these are powerful and general models, as mentioned previously, they currently only consider cannulas in free space.

The purpose of our paper is to extend these models to describe the shape of an active cannula when external forces and torques are applied to it. We then provide experimental validation of this framework. These results provide the theoretical foundation necessary for model-based control and force sensing using the cannula itself as a force sensor, as was recently accomplished for flexible, push-rod driven, continuum robots by Xu and Simaan [14].

Fig. 1: An active cannula consisting of three concentric, telescoping, precurved Nitinol tubes. Cannula shape can be controlled by rotating and translating the tubes at their bases.

II. MECHANICS-BASED MODEL

A. Assumptions and Kinematics

All derivations in this paper take place under the standard assumptions of Kirchoff rod theory, a special case of Cosserat rod theory (see [15] for an in-depth treatment of both). Kirchoff theory assumes inextensibility and neglects transverse shear – which are generally regarded as good assumptions for long thin rods such as the tubes used in most prototype active cannulas. We use the linear Bernoulli-Euler constitutive law ((6) in Section II-B). We also neglect friction in this paper, as do all active cannula models to date. The low tip errors found in the experimental section indicate that this is a reasonable assumption for our active cannula prototype.

To describe the kinematics of a curved robot, we begin by considering a single unloaded curved tube. Let the shape of the tube be defined by an arc-length parameterized Cartesian curve $r_i^*(s)$[1]. We assign frames continuously along $r_i^*(s)$, and by convention choose the z axes of these frames to always be tangent to the curve. These frames may be attached with any framing convention where their z axes are tangent to the curve, e.g. Bishop's frames or Frenet-Serret frames. Framing the initial tube curve creates a rotation matrix $R_i^*(s)$ at every arc length location s on the undeformed curve, thus establishing an arc length parametrized transformation $g_i^*(s)$ along the tube,

$$g_i^*(s) = \begin{bmatrix} R_i^*(s) & r_i^*(s) \\ \mathbf{0} & 1 \end{bmatrix}^T. \tag{1}$$

The local curvature vector is established by the well-known relationship

$$u_i^*(s) = \left(R_i^{*T}(s)\dot{R}_i^*(s) \right)^\vee, \tag{2}$$

where the dot here denotes a derivative with respect to arc length s. The $^\vee$ operator denotes conversion of an element of $\mathfrak{so}(3)$ (the Lie algebra of $SO(3)$) to its corresponding element in $\mathbb{R}^3$. Following convention, we "overload" the $^\vee$ notation so that it also indicates the mapping from $\mathfrak{se}(3)$ (the Lie algebra of $SE(3)$) to $\mathbb{R}^6$. The $^\wedge$ operator denotes the inverse operation in both cases (see [16] for a thorough discussion of this notation).

Because the tubes in this collection are arranged concentrically, the tangent vectors of each deformed tube in the collection must be equal at s, thus each $R_i(s)$ differs from the others by a rotation about the local tangent z axis. We introduce an angle $\theta_i(s)$ to parameterize this difference as

$$R_i(s) = R_1(s)R_{\theta_i} \tag{3}$$

where $R_{\theta_i} = e^{\hat{e}_3\theta_i(s)}$ denotes a rotation about the z axis by $\theta_i(s)$, and $\theta_1 \equiv 0$ by definition. We use this to obtain a relationship between the tube curvature vectors which

¹Note that throughout the paper, we use the * to denote variables associated with undeformed individual tube shapes. Thus, $r_i^*(s)$ indicates the pre-set shape a single tube would have in the absence of any other tubes or external loads.
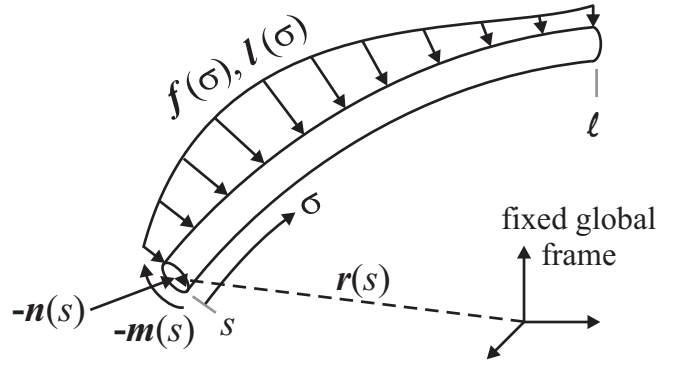

Fig. 2: Section of rod from s to the free end ℓ subject to distributed forces and moments. The internal force and moment are also shown.

enforces the tangency constraint. Applying the definition of u_i, we get

$$u_i = \left(R_i^T \dot{R}_i \right)^\vee = R_{\theta_i}^T u_1 + \dot{\theta}_i e_3. \tag{4}$$

Given u_i, the deformed curve can be constructed by integrating $g_i(s)$ using

$$\dot{g}_i(s) = g_i(s)\hat{\xi}_i(s). \tag{5}$$

where $\xi_i(s) = \begin{bmatrix} 0 & 0 & 1 & u_i^T(s) \end{bmatrix}^T$.

B. Mechanics of a Collection of Tubes under Load

Neglecting elongation and transverse shear, any deformation of a tube from its initial state $g_i^*(s)$ to a new state $g_i(s)$ can be described by a corresponding change from $u_i^*(s)$ to $u_i(s)$, which we denote $\Delta u_i(s) = u_i(s) - u_i^*(s)$. The Bernoulli-Euler constitutive law can then be used to describe the relationship of the strain variables to the internal moment at s:

$$M_i(s) = K_i(s)\Delta u_i(s), \tag{6}$$

where $K_i(s) = \text{diag}\{E_i(s)I_i(s) \quad E_i(s)I_i(s) \quad G_i(s)J_i(s)\}$, and $M_i(s)$ is the moment expressed in the local frame.

We consider a single tube extending from arc length $s = 0$ to $s = \ell$ and subject to an arbitrary combination of distributed forces $f(s)$ and moments $l(s)$ along its length. We then cut a section of this tube at an arbitrary arc length location s, as shown in Fig. 2. By convention, we denote the internal force which the material of $[s, \ell]$ exerts on the material of $[0, s)$ as $n(s)$, expressed in the global frame. Similarly, the internal moment which the material of $[s, \ell]$ exerts on the material of $[0, s)$ is $m(s)$, expressed in the global frame. Summing the forces on the portion $[s, \ell]$ we have,

$$\int_s^\ell f(\sigma)d\sigma - n(s) = 0. \tag{7}$$

Similarly, summing the moments on the portion $[s, \ell]$ about the world frame origin, we obtain

$$\int_s^\ell \left(r(\sigma) \times f(\sigma) + l(\sigma) \right) d\sigma - m(s) - r(s) \times n(s) = 0. \tag{8}$$

To generalize (7) and (8) to a cannula with multiple tubes, we will have one force distribution $\boldsymbol{f}_i(s)$, and one moment distribution $\boldsymbol{l}_i(s)$, per tube. The assumptions of shearlessness and inextensibility allow us to consider the sum of all force distributions applied to specific tubes as a single force distribution applied to the collective backbone, $\sum_{i=1}^n \boldsymbol{f}_i(s) = \boldsymbol{f}(s)$. However, this is not the case with moments, since the tubes can axially rotate independently of one another. For this reason we must retain the i subscripts on the moment distributions $\boldsymbol{l}_i(s)$ to distinguish the tube to which these moment distributions are physically applied. Thus, summing forces for a collection of tubes we have

$$\int_s^\ell \boldsymbol{f}(\sigma)d\sigma - \sum_{i=1}^n \boldsymbol{n}_i = 0, \qquad (9)$$

and summing moments we have,

$$\int_s^\ell \left(\boldsymbol{r}(\sigma) \times \boldsymbol{f}(\sigma) + \sum_{i=1}^n \boldsymbol{l}_i(\sigma) \right) d\sigma$$
$$- \sum_{i=1}^n \left(\boldsymbol{m}_i(s) - \boldsymbol{r}(s) \times \boldsymbol{n}_i(s) \right) = 0. \qquad (10)$$

Taking the derivative of (9) with respect to s, we obtain

$$\sum_{i=1}^n \dot{\boldsymbol{n}}_i + \boldsymbol{f} = 0, \qquad (11)$$

where we have dropped the explicit dependence on (s) to simplify notation, as we will continue to do for the remainder of the paper, except where needed for clarity. Similarly, taking the derivative of (10) with respect to s and substituting in (11) yields

$$\sum_{i=1}^n \left(\dot{\boldsymbol{m}}_i + \dot{\boldsymbol{r}} \times \boldsymbol{n}_i + \boldsymbol{l}_i \right) = 0. \qquad (12)$$

Equations 11 and 12 are multi-tube analogues of the single Cosserat equilibrium equation as derived in [15]. We now proceed to expand (12) and solve for $\dot{\boldsymbol{u}}_i$ in terms of the precurvatures and applied loads. We use the constitutive law (6) for each tube, the frame transformations $\boldsymbol{m}_i = R_i \boldsymbol{M}_i$, $\boldsymbol{n}_i = R_i \boldsymbol{N}_i$, and the kinematic relationship $\dot{R}_i = R_i \hat{\boldsymbol{u}}_i$ to write

$$\sum_{i=1}^n \dot{\boldsymbol{m}}_i(s) = \sum_{i=1}^n R_i \Big(K_i \left(\dot{\boldsymbol{u}}_i - \dot{\boldsymbol{u}}_i^* \right)$$
$$+ (\hat{\boldsymbol{u}}_i K_i + \dot{K}_i)\left(\boldsymbol{u}_i - \boldsymbol{u}_i^* \right) \Big). \qquad (13)$$

Since the tubes' common tangent vector at s is the z axis of the attached frame, we use $\dot{\boldsymbol{r}} = R_1 \boldsymbol{e}_3$ and (9) to write the last two terms of (12) in terms of the applied loads as

$$\sum_{i=1}^n \left(\dot{\boldsymbol{r}} \times \boldsymbol{n}_i + \boldsymbol{l}_i \right) = R_1 \boldsymbol{e}_3 \times \int_s^\ell \boldsymbol{f}(\sigma)d\sigma + \sum_{i=1}^n \boldsymbol{l}_i. \qquad (14)$$

Then, after pre-multiplying by $R_1^T(s)$ and recalling that $R_{\theta_i} = R_1^T(s)R_i(s)$ from (3), (12) becomes

$$\sum_{i=1}^n R_{\theta_i} \Big(K_i \left(\dot{\boldsymbol{u}}_i - \dot{\boldsymbol{u}}_i^* \right) + (\hat{\boldsymbol{u}}_i K_i + \dot{K}_i)\left(\boldsymbol{u}_i - \boldsymbol{u}_i^* \right) \Big)$$
$$+ \boldsymbol{e}_3 \times R_1^T \int_s^\ell \boldsymbol{f}(\sigma)d\sigma + R_1^T \sum_{i=1}^n \boldsymbol{l}_i = 0. \qquad (15)$$

In order to integrate, we wish to obtain an expression for $\dot{\boldsymbol{u}}_1$ in terms of only the other state variables $\boldsymbol{u}_1, ... \boldsymbol{u}_n$. So we substitute in the derivative of (4),

$$\dot{\boldsymbol{u}}_i(s) = \dot{\theta}_i \frac{dR_{\theta_i}^T}{d\theta_i} \boldsymbol{u}_1 + R_{\theta_i}^T \dot{\boldsymbol{u}}_1 + \ddot{\theta}_i \boldsymbol{e}_3, \qquad (16)$$

to eliminate $\dot{\boldsymbol{u}}_2, ... \dot{\boldsymbol{u}}_n$. This substitution enables us to solve (15) for the first two components, $\dot{u}_{1,x}$ and $\dot{u}_{1,y}$ in terms of $\boldsymbol{u}_1, ... \boldsymbol{u}_n$:

$$\begin{bmatrix} \dot{u}_{1,x} \\ \dot{u}_{1,y} \end{bmatrix} = -K^{-1} \sum_{i=1}^n R_{\theta_i} \Big(K_i (\dot{\theta}_i \frac{dR_{\theta_i}^T}{d\theta_i} \boldsymbol{u}_1 - \dot{\boldsymbol{u}}_i^*)$$
$$+ (\hat{\boldsymbol{u}}_i K_i + \dot{K}_i)(\boldsymbol{u}_i - \boldsymbol{u}_i^*) \Big) \Big|_{x,y}$$
$$- K^{-1} \Big(\boldsymbol{e}_3 \times R_1^T \int_s^\ell \boldsymbol{f}(\sigma)d\sigma + R_1^T \sum_{i=1}^n \boldsymbol{l}_i \Big) \Big|_{x,y} \qquad (17)$$

where $K = \sum_{i=1}^n K_i$ and $|_{x,y}$ denotes selection of only the first two components of a vector. It is not possible to write $\dot{u}_{1,z}$ in terms of $\boldsymbol{u}_1, ... \boldsymbol{u}_n$ using only (15) and (16).

It is possible, however, to derive a relationship for the torsional components via minimizing the total elastic energy stored in the collection of tubes. Using the constitutive equation (6), the elastic energy stored in the n tube deformations is

$$E = \frac{1}{2} \sum_{i=1}^n \int_0^\ell (\boldsymbol{u}_i - \boldsymbol{u}_i^*)^T K_i (\boldsymbol{u}_i - \boldsymbol{u}_i^*)ds. \qquad (18)$$

Substituting in (4) we have

$$E = \frac{1}{2} \int_0^\ell \boldsymbol{u}_1^T K_1 \boldsymbol{u}_1 - 2\boldsymbol{u}_1^T K_1 \boldsymbol{u}_1^* + \boldsymbol{u}_1^{*T} K_1 \boldsymbol{u}_1^*$$
$$+ \sum_{i=2}^n \Big(\boldsymbol{u}_1^T K_i \boldsymbol{u}_1 + 2\boldsymbol{u}_1^T K_i \dot{\theta}_i \boldsymbol{e}_3 - 2\boldsymbol{u}_1^T R_{\theta_i} K_i \boldsymbol{u}_i^*$$
$$+ \boldsymbol{u}_i^{*T} K_i \boldsymbol{u}_i^* - 2\boldsymbol{u}_i^{*T} K_i \dot{\theta}_i \boldsymbol{e}_3 + \dot{\theta}_i^2 \boldsymbol{e}_3^T K_i \boldsymbol{e}_3 \Big)ds. \qquad (19)$$

To find the functions θ_i which minimize the stored elastic energy, we apply the Euler–Lagrange equation shown below to the functional $n-1$ times, once with respect to each θ_i:

$$\frac{\partial f}{\partial \theta_i} - \frac{d}{ds}\left(\frac{\partial f}{\partial \dot{\theta}_i} \right) = Q_i'. \qquad (20)$$

Note that the right hand side is not zero as is the case in prior free space models [13]. Instead we have Q_i', which represents any generalized forces associated with θ_i. In this case, they are the arc length parametrized torque per unit

length applied along the e_3 axis of tube i. Applying the Euler–Lagrange equation to the functional, we obtain

$$- \boldsymbol{u}_1^T \frac{\partial R_{\theta_i}}{\partial \theta_i} K_i \boldsymbol{u}_i^* - (\dot{\boldsymbol{u}}_1 - \dot{\boldsymbol{u}}_i^*)^T K_i \boldsymbol{e}_3 - (\boldsymbol{u}_1 - \boldsymbol{u}_i^*)^T \dot{K}_i \boldsymbol{e}_3$$
$$- \ddot{\theta}_i \boldsymbol{e}_3^T K_i \boldsymbol{e}_3 - \dot{\theta}_i \boldsymbol{e}_3^T \dot{K}_i \boldsymbol{e}_3 = \boldsymbol{e}_3 R_i(s) l_i(s). \tag{21}$$

Using (4) and its derivative to replace $\boldsymbol{u}_1$ and $\dot{\boldsymbol{u}}_1$, we solve for $\dot{\boldsymbol{u}}_{i,z}$ and obtain,

$$\dot{\boldsymbol{u}}_{i,z} = \dot{\boldsymbol{u}}_{i,z}^* + \frac{E_i I_i}{G_i J_i} (\boldsymbol{u}_{i,x} \boldsymbol{u}_{i,y}^* - \boldsymbol{u}_{i,y} \boldsymbol{u}_{i,x}^*)$$
$$+ \frac{(\dot{G_i J_i})}{G_i J_i} (\boldsymbol{u}_{i,z}^* - \boldsymbol{u}_{i,z}) - \frac{1}{G_i J_i} \boldsymbol{e}_3^T R_i^T \boldsymbol{l}_i. \tag{22}$$

The equation is independent of the loads that the other tubes apply to tube i except for any directly applied axial moments at s, which are necessarily zero under the assumption of no static friction between tubes. A version of (22) without the last two terms was derived in [11] using a different approach, and without considering external loading. We can now use (22) for $i = 1$ to get $\dot{\boldsymbol{u}}_{1,z}$.

C. Model Implementation

The set of variables to be integrated to obtain the final backbone shape is $\{g_1, \boldsymbol{u}_{1,x}, \boldsymbol{u}_{1,y}, \boldsymbol{u}_{1,z}, \boldsymbol{u}_{2,z}, ..., \boldsymbol{u}_{n,z}\}$. Their derivatives are defined by (17), (22), and (5), while (4) can be used to calculate $\boldsymbol{u}_i$ from $\boldsymbol{u}_1$ at every step. For convenience, (17) and (4) are written in terms of θ_i and $\dot{\theta}_i$. The latter can be obtained from the state variables at every step using $\dot{\theta}_i = \boldsymbol{u}_{i,z} - \boldsymbol{u}_{1,z}$, which follows from (4), and θ_i can be obtained by integrating $\dot{\theta}_i$.

The unknown boundary conditions at the proximal end are the initial curvature values $\{\boldsymbol{u}_{1,x}(0), \boldsymbol{u}_{1,y}(0), \boldsymbol{u}_{1,z}(0), \boldsymbol{u}_{2,z}(0), ..., \boldsymbol{u}_{n,z}(0)\}$. At the distal end, one boundary condition is that the sum of the internal moments vanishes (assuming no point moments applied at the tip), $\sum_{i=1}^{n} \boldsymbol{m}_i(\ell) = 0$. Also, the axial component of each tube's internal moment must vanish at its tip, $\boldsymbol{e}_3^T \boldsymbol{M}_i(\ell_i) = 0$. Continuity of the total internal moment $\sum_{i=1}^{n} \boldsymbol{m}_i(s) = 0$ must also be maintained across locations where tubes end or become curved. In our experiments, we employ a standard shooting method to solve for the values of the unknown initial curvatures which satisfy the boundary conditions at the distal end.
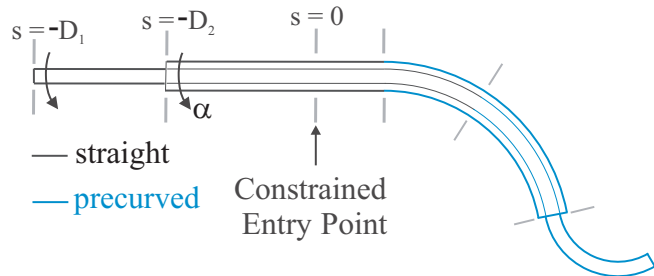

Fig. 3: A Diagram of the experimental two tube cannula. The point of entry into the workspace is designated as the arc length zero datum.
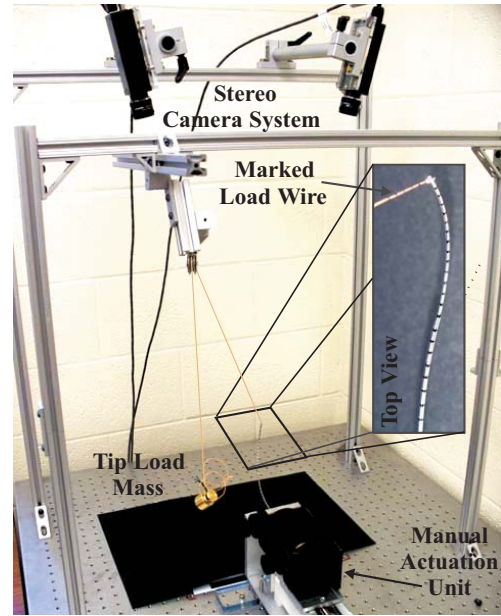

Fig. 4: A photo of the experimental setup. Tube bases were translated and rotated precisely by manual actuators, and positions along the backbone were triangulated using the stereo camera system. The applied force vector was measured in the same way.

TABLE I: Measured and Assumed Physical Quantities for Experimental Tubes

	Tube 1 (Inner)	Tube 2 (Outer)
Inner Diameter (mm)	1.25	2.00
Outer Diameter (mm)	1.75	2.37
Straight Length (mm)	122.7	30.7
Curved Length (mm)	206.9	102.5
Young's Modulus (E) (GPa)	60	60
Shear Modulus (G) (GPa)	23.1	23.1

III. EXPERIMENTS

In order to validate the model developed in Section II, a set of experiments was performed for a collection of two precurved Nitinol tubes in various configurations subject to various tip loads.

A. Tube Properties and Measurement Procedure

The physical properties of the tubes used are given in Table I, and they are shown schematically in Fig. 3. The curvature values were computed as described below and are shown in Fig. 5. The outer tube was held stationary in its fully extended position, while the base of the inner tube was translated to 5 different positions, given in Table II. At each of these translational positions, the inner tube was rotated to 8 evenly spaced angular positions, given in Table III

Thus, the tubes were actuated to 40 different workspace locations which evenly span the set of angular and linear differences of the tubes' base positions. Using this set of configurations, a set of tip points that spans the entire

workspace of the cannula can be generated by a rigid rotation of both tubes about the z axis. Thus, this set of configurations represents a sampling of all unique (from the model's point of view) positions in the configuration space of the cannula.

As shown in Fig. 4, at each of these configurations, a set of 3D points along the backbone was obtained from images taken using a calibrated pair of stereo cameras (Sony XCD-X710 Firewire cameras with a resolution of 1024×768 pixels). The fiducial markers shown in the inset image in Fig. 4 enabled determination of point correspondences for stereo triangulation. To facilitate this, each fiducial was manually identified in image coordinates by clicking on the center of the black bands in each image using MATLAB's `ginput`. The transformation between the stereo camera coordinate frame and the cannula base frame was estimated using point cloud registration [17] using a grid of points, the position of which could be measured with calipers in the cannula frame and triangulated in the stereo camera frame.

For each of the 40 actuator configurations, a point force was then applied by a wire tied through a hole in the tip of the inner tube. The force vector applied by this wire was also determined by manually clicking marked points along its length. The wire was run over a pulley as shown in Fig. 4 and attached to a mass ranging from 100 g to 500 g as detailed in Table II. Backbone data was then also taken in the loaded state. Thus our total experimental dataset consisted of 40 unloaded configurations and the same 40 configurations with tip forces applied.

The two tubes have general precurvatures $\boldsymbol{u}_1^*(s)$ and $\boldsymbol{u}_2^*(s)$ which were calculated analytically from a parametric curve that was fit to points along the tube. These points were triangulated for each tube individually using the same procedure described previously for collecting the shape of the entire cannula. We note that these tubes are not circularly precurved, as has been the case with all prior prototypes in the literature. Fig. 5 illustrates that the measured curvatures are general and change significantly along the arc length.

B. Model Performance and Parameter Fitting

Using the nominal parameter values (those that can be measured or appear on data sheets – see [9] for further discussion of active cannula nominal parameters, variances,

TABLE II: Translational Actuator Configurations

D_1 (mm)	131.7	154.7	177.7	200.7	223.7
D_2 (mm)	30.7	30.7	30.7	30.7	30.7
Tip Load (N)	0.981	0.981	0.981	1.962	4.905[1]

[1] For $\alpha_1 = 0°$, $\alpha_2 = 0°$, $D_1 = 223.7$ mm, the load was 1.962N.

TABLE III: Rotational Actuator Positions Applied at Each Translational Configuration Shown in Table II

α_1 (deg)	0	45[1]	90	135	180	225	270	315
α_2 (deg)	0	0	0	0	0	0	0	0

[1] $\alpha_1 = 60°$ was substituted for $\alpha_1 = 45°$ when $D_1 = 131.7$ mm to keep the tip of the cannula in the field of view of both cameras.
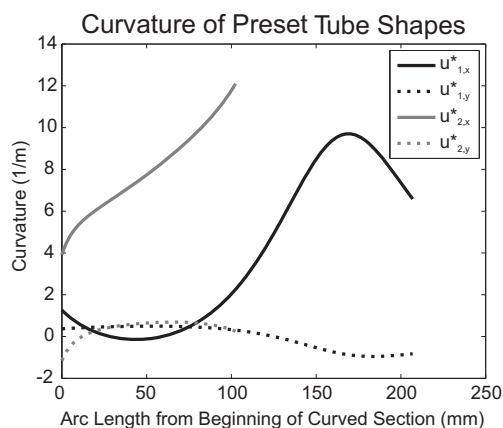

Fig. 5: Measured curvatures of the preset tube shapes expressed in Rotation Minimizing (Bishop's) frames. Only the x and y components are shown because this frame convention requires $\boldsymbol{u}_{1,z}^* = \boldsymbol{u}_{2,z}^* = 0$.

and error propagations) of E_1, E_2, G_1 and G_2 and measured inner and outer diameters listed in Table I, the mean error in tip position over all 80 experiments was 5.79 mm. Since actual values for the moduli of Nitinol tubes are uncertain (they are listed as 41–75 GPa on data sheets from the manufacturer, NDC, Inc.), the values of each tube's bending and torsional stiffness were subsequently calibrated by minimizing the sum of the positional errors at the base ($s = 0$), the tip of tube 2, and the tip of tube 1. To account for small errors in registration between the model and experimental cannula position, the robot base frame (described by XYZ Euler angles and translation) was included in the calibration
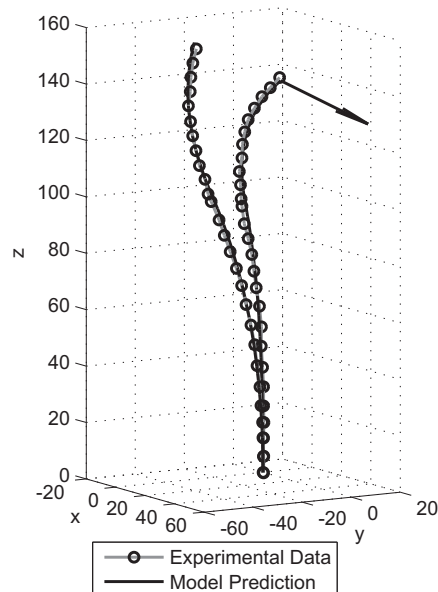

Fig. 6: Comparison of model prediction and experimentally determined backbone points for the unloaded and loaded cases where $D_1 = -154.7$, $D_2 = -30.7$, $\alpha_1 = 135°$, and $\alpha_2 = 0°$. The arrow shows the direction of the 0.981 N applied force. The tip error in both cases (about 3 mm) is representative of the mean tip error for all 80 cases.

TABLE IV: Nominal and Calibrated Tube Stiffnesses

	Nominal Value	Calibrated Value
$E_1 I_1$ (Nm^2)	0.0204	0.0197
$J_1 G_1$ (Nm^2)	0.0157	0.0123
$E_2 I_2$ (Nm^2)	0.0458	0.0368
$J_2 G_2$ (Nm^2)	0.0352	0.0331

TABLE V: Tip Error Statistics For Nominal Parameters

Tip Error Statistic (mm)	40 Unloaded Cases	40 Loaded Cases	All Cases
mean	3.76	7.82	5.79
min	0.60	2.42	0.60
max	10.59	25.53	25.53
std. dev.	2.85	4.13	4.08

TABLE VI: Tip Error Statistics For Fitted Parameters

Tip Error Statistic (mm)	40 Unloaded Cases	40 Loaded Cases	All Cases
mean	2.89	2.92	2.91
min	0.62	0.91	0.62
max	8.49	15.20	15.20
std. dev.	2.19	2.52	2.34

procedure and initialized with the results from the point cloud registration. The optimization was done using MATLAB's `fminsearch` function, which performs Nelder-Meade simplex unconstrained optimization.

These calibrated parameters are shown in comparison to their nominal counterparts in Table IV. The robot base showed only small changes during optimization, moving through XYZ Euler angles of $-0.06°$, $0.67°$, and $-0.58°$, with the position of the base frame origin translating 2.0 mm. Using these fitted parameter values, the mean error over all experiments was reduced to 2.91 mm.

Fig. 6 shows the unloaded and loaded states of the cannula where the actuator values are $D_1 = -154.7$, $D_2 = -30.7$, $\alpha_1 = 135°$, and $\alpha_2 = 0°$. The experimental data are shown overlaid on the model prediction with calibrated parameters. This configuration is typical of all 80 experimental configurations in that the tip error in both cases is about 3 mm, while the mean for all experiments was 2.91 mm. The rest of the shape is also typical of the 80 experimental configurations in that the experimental data lies very close to the model prediction along the entire backbone.

Error statistics for both nominal and fitted parameters are given in Tables V and VI. The maximum error of 15.20 mm is an outlier (the second highest error is less than 9 mm). The outlier appears to have been caused by an unintentionally applied moment at the tip, due to the way the wire was wrapped around the side of the tube in that particular configuration. Other loaded experiment tip errors in the 5-8 mm range occur in configurations where the applied load was slightly wrapped around the side of the cannula tip to reach the pulley, and thus may have applied small unintended moments in addition to the desired forces.

IV. CONCLUSIONS

In this paper we presented use of geometrically exact Kirchoff rod theory to describe the shape of a collection of concentric precured tubes under general force and moment distributions. We also presented experimental studies applying the model to a prototype active cannula, with average error of 2.91 mm in 80 configurations with varying tip loads.

This model extends the use of active cannulas to applications where they must interact with tissue. It provides the foundation for model-based position and force control of active cannulas under external loads. We also anticipate using this modeling framework in future work to enable use of the cannula itself as a force sensor.

REFERENCES

[1] R. J. Webster III, "Design and mechanics of continuum robots for surgery," Mechanical Engineering, Johns Hopkins University, Baltimore, MD, December 2007, PhD Thesis.

[2] D. C. Rucker, J. M. Croom, and R. J. Webster III, "Aiming surgical lasers with an active cannula," *ASME Journal of Medical Devices*, vol. 3, no. 2, p. 027506, 2009.

[3] D. Trivedi, A. Lotfi, and C. Rahn, "Geometrically exact models for soft robotic manipulators," *IEEE Transactions on Robotics*, vol. 24, pp. 773 – 780, 2008.

[4] I. A. Gravagne, C. Rahn, and I. D. Walker, "Large-deflection dynamics and control for planar continuum robots," *IEEE/ASME Transactions on Mechatronics*, vol. 8, no. 2, pp. 299–307, June 2003.

[5] M. Terayama, J. Furusho, and M. Monden, "Curved multi-tube device for path-error correction in a needle-insertion system," *International Journal of Medical Robotics and Computer Assisted Surgery*, vol. 3, no. 2, pp. 125–134, 2007.

[6] R. J. Webster III, A. M. Okamura, and N. J. Cowan, "Toward active cannulas: Miniature snake-like surgical robots," *IEEE/RSJ International Conference on Intelligent Robots and Systems*, pp. 2857–2863, 2006.

[7] P. Sears and P. E. Dupont, "A steerable needle technology using curved concentric tubes," *IEEE/RSJ International Conference on Intelligent Robots and Systems*, pp. 2850–2856, 2006.

[8] ——, "Inverse kinematics of concentric tube steerable needles," *IEEE International Conference on Robotics and Automation*, pp. 1887–1892, 2007.

[9] R. J. Webster III, J. M. Romano, and N. J. Cowan, "Mechanics of precurved-tube continuum robots," *IEEE Transactions on Robotics*, vol. 25, no. 1, pp. 67–78, 2009.

[10] D. C. Rucker and R. J. Webster III, "Mechanics-based modeling of bending and torsion in active cannulas," *IEEE RAS/EMBS International Conference on Biomedical Robotics and Biomechatronics*, pp. 704–709, 2008.

[11] P. Dupont, J. Lock, and E. Butler., "Torsional kinematic model for concentric tube robots," *IEEE International Conference on Robotics and Automation*, pp. 3851 – 3858, 2009.

[12] D. C. Rucker, R. J. Webster III, G. S. Chirikjian, and N. J. Cowan, "Equilibrium conformations of concentric-tube continuum robots," *International Journal of Robotics Research*, 2010, (Accepted).

[13] D. C. Rucker and R. J. Webster III, "Parsimonious evaluation of concentric-tube continuum robot equilibrium conformation," *IEEE Transactions on Biomedical Engineering*, vol. 56, pp. 2308 – 2311, 2009.

[14] K. Xu and N. Simaan, "An investigation of the intrinsic force sensing capabilities of continuum robots," *IEEE Transactions on Robotics*, vol. 24, no. 3, pp. 576–587, 2008.

[15] S. S. Antman, *Nonlinear Problems of Elasticity*, 2nd ed., S. Antman, J. Marsden, and L. Sirovich, Eds. Springer Science, 2005.

[16] R. M. Murray, Z. Li, and S. S. Sastry, *A Mathematical Introduction to Robotic Manipulation*. Boca Raton, FL: CRC Press, 1994.

[17] K. S. Arun, T. S. Huang, and S. D. Blostein, "Least-squares fitting of two 3-D point sets," *IEEE Transactions on Pattern Analysis and Machine Intellegence*, vol. 9, no. 5, pp. 698–700, 1987.